Available online at www.sciencedirect.com
ScienceDirect
Trans. Nonferrous Met. Soc. China 34(2024) 1533−1546
Transactions of Nonferrous Metals Society of China
www.tnmsc.cn

Effect of Cr coating on creep behavior of zircaloy-4 alloy

Ding ZUO[1], Pei-nan DU[2], Wei LUO[1], Huan CHEN[2],
Yu WANG[2], Tian-guo WEI[2], Rui-qian ZHANG[2], Hui-qun LIU[1,3]

1. School of Materials Science and Engineering, Central South University, Changsha 410083, China;
2. Science and Technology on Reactor Fuel and Materials Laboratory, Nuclear Power Institute of China, Chengdu 610213, China;
3. State Key Laboratory of Powder Metallurgy, Central South University, Changsha 410083, China

Received 31 December 2022; accepted 12 June 2023

Abstract: The effects of Cr coating, deposited by chemical vapor deposition, on the creep properties of Zr-4 alloy and the results for its stability during long-time service were reported. Its microstructure was studied by scanning electron microscopy, electron probe microanalysis, and electron backscatter diffraction. Results show that the grains of the Zr-4 matrix were equiaxed, exhibiting ⟨0001⟩ texture parallel to the normal direction (⟨0001⟩//ND). Moreover, after the creep test, coated samples displayed a lower number of subgrain boundaries within their matrix compared with uncoated samples. Thus, the application of a Cr coating is instrumental in minimizing the stress on Zr-4, ultimately contributing to an enhancement in creep resistance of the coated samples. The Cr coating exhibits a high stability during long-term diffusion test. The coating cracks at a minimum stress of 157 MPa at 350 °C and 137 MPa at 400 °C. The Monkman−Grant relationship between the steady-state creep rate and creep fracture time was derived using a systematic summary of data pertaining to creep fracture.

Key words: Zr-4 alloy; Cr coating; creep behavior; microstructure; thermal stability

1 Introduction

Zirconium (Zr) alloy is one of the most important raw materials for fuel cladding tubes and structural components in nuclear reactors. This can be attributed to its favorable characteristics, such as low neutron capture cross-sections, satisfactory mechanical behavior, and exceptional resistance to corrosion. Consequently, Zr alloys have become a preferred option for various applications in the nuclear energy sector. The preeminent cladding materials in pressurized water reactors are zircaloy-2 (Zr-2) and zircaloy-4 (Zr-4). Zr-4, procured by reducing the Ni content from Zr-2 and augmenting the Fe content, exhibits inferior hydrogen absorption capacity than Zr-2 [1]. To establish the dependability of zirconium alloys employed in nuclear reactors, a series of experiments were executed to appraise their efficacy in regard to oxidation resistance, hydrogen absorption, creep resistance, and property degradation [2−4]. The investigations revealed that the performance of Zr alloys, notably Zr-4, satisfies the prerequisites for extended operation in nuclear reactors. However, during loss-of-coolant accidents, the Zr-clad tube may not retain its structural integrity and could react with high-temperature water, leading to the release of large amounts of hydrogen gas, potentially resulting in an explosion. The Fukushima nuclear accident that occurred in 2011 proved that the currently used Zr alloy-based

Corresponding author: Hui-qun LIU, Tel: +86-13975809193, E-mail: liuhuiqun@csu.edu.cn
DOI: 10.1016/S1003-6326(24)66489-7

cladding materials pose significant security risks in catastrophic incidents.

To improve the accident tolerance, extensive research has been conducted on the accident-tolerant fuels, primarily focusing on cladding materials [5−7]. Two strategies have been proposed to improve the performance of cladding materials. The first approach involves the deposition of a protective coating onto the surface of the Zr alloy, whereas the second entails exploring alternative materials, such as SiC_f/SiC composites [8,9] and FeCrAl stainless steel [10,11], as potential replacements for Zr alloy in the role of cladding material [12]. Of these two strategies, the former offers the advantage of requiring minimal alteration to the existing nuclear fuel structure design, rendering it a less hazardous and more viable option for near-term implementation.

Conventional high-temperature coatings depend on the formation of an unbroken, self-protective oxide layer on the surface. The common oxide layers are Cr_2O_3, Al_2O_3, and SiO_2 [13,14], of which Al_2O_3 and SiO_2 have higher maximum temperature thresholds; however, both of these materials show chemical instability when used in water-cooled reactors [15,16], whereas Cr_2O_3-generating materials are more reliable when used as coatings on Zr alloy claddings. The feasibility of Cr_2O_3-generating materials, such as CrN, MAX phase, and Cr [15,17], have been evaluated and Cr has been identified as suitable for use as a coating for Zr alloy cladding [18,19]. Studies on Cr coating for Zr alloys have demonstrated that it significantly improves the corrosion resistance of Zr alloys [20,21] and demonstrates irradiation stability [22], good steam oxidation resistance [23,24], and lower high-temperature diffusion [25,26]. However, to date, there has been limited research on the creep behavior of Cr-coated Zr alloy and its underlying mechanisms.

For the Zr-4 alloy, a phenomenological relationship has been established between stress and creep rate. When the creep deformation shows a non-linear dependence on creep time, the obtained creep deformation−time curve can be divided into three stages. In primary creep (Stage I), the creep rate ($\dot{\varepsilon}=\mathrm{d}\varepsilon/\mathrm{d}t$) decreases with increasing creep time up to a certain value. Secondary creep, also known as steady-state creep (Stage II), occurs when the creep rate is constant and comprises the majority of the creep life. During this period, the creep of the alloy follows a power law:

$$\dot{\varepsilon}=A\sigma_0^n\exp\left(-\frac{\Delta E}{RT}\right) \tag{1}$$

where $\dot{\varepsilon}$ is the strain rate, σ_0 is the applied stress, A and n (stress exponent) are constants, ΔE is the molar activation enthalpy, R is the molar gas constant, and T is the thermodynamic temperature. As the creep progresses, the creation of cavities or cracks significantly increases the creep rate, leading to tertiary creep. In tertiary creep (Stage III), the creep rate increases until creep fracture occurs.

Creep fracture in uniaxial tension under constant stress has been described by the Monkman−Grant relationship [27]:

$$\dot{\varepsilon}_{ss}N_{t_f}=k_{MG} \tag{2}$$

where $\dot{\varepsilon}_{ss}$ is the steady-state creep rate, t_f is the fracture time, N is a constant that is typically equal to approximately 1.0, and k_{MG} is the Monkman–Grant constant. This phenomenological relationship can be fitted suitably to the data obtained from the accelerated creep fracture under higher stress levels [28].

This study aimed to investigate the effect of Cr coating on the creep behavior of Zr-4 alloy and reveal creep mechanisms. The creep parameters were established based on previous investigations [29] on the creep behavior of Zr alloy, and higher stress was applied to accelerating the creep process for the study of creep fracture. Finally, a failure analysis of the coating was conducted to assess its viability at the designated service temperature.

2 Experimental

Zr-4 plates, which were cold-rolled with a reduction of 30% and subsequently annealed at 580 °C for 12 h, were obtained from the Nuclear Power Institute of China. The nominal compositions of Zr-4 and results of the inductively coupled plasma spectrometry measurements are listed in Table 1. The Zr-4 plates were machined to a dog-bone shape (Fig. 1, gauge length: 35 mm, thickness: 4.5 mm) and a small cube (4.5 mm × 4 mm × 4 mm) for further coating. A Cr coating with a thickness of approximately 20 μm was deposited onto the Zr-4 plates using chemical vapor deposition (CVD). The matrices were polished

using SiC papers, ultrasonicated in acetone, and subsequently dried with cold air. We refer to the sample after CVD treatment as the as-received sample.

Creep tests were conducted using a high-temperature creep testing machine (RDL30), which consists of a high-temperature furnace, three thermocouples, a tie rod to provide uniaxial stress, and a deformation sensor to observe real-time deformation, as shown in Fig. 1. The creep conditions, primary creep strain, total strain, steady-state creep rate, and creep time are listed in Table 2.

Table 1 Chemical composition of Zr-4 alloy (wt.%)

Element	Nominal	ICP tested
Sn	1.5	1.35
Fe	0.2	0.21
Cr	0.1	0.094
Zr	Bal.	Bal.

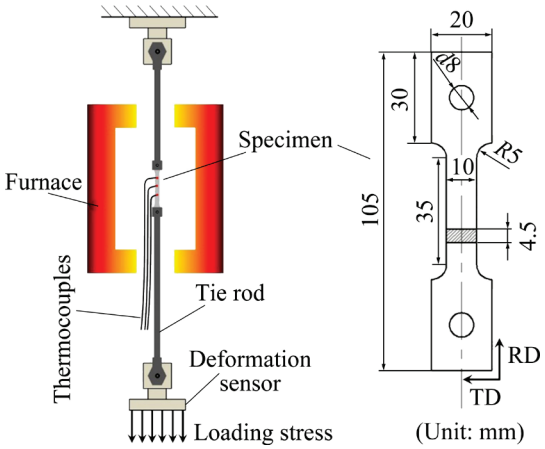

Fig. 1 Schematic diagram of creep test device

To evaluate the diffusion between the coating and Zr-4 matrix, a diffusion test was performed on the coated sample at 400 °C for 1000 h in a muffle furnace, wherein the samples were encapsulated in a quartz tube filled with nitrogen gas to prevent high-temperature oxidation.

Scanning electron microscopy (SEM, TESCAN MIRA4 LMH) was employed to characterize the microstructures of the coating surface and coating-matrix bonding interface. The samples were first ground using increasingly fine SiC papers with grit sizes of 180, 240, 320, 400, 600, 800, and 1000 and then with increasingly fine metallographic sandpapers with grit sizes of 400, 600, and 800, followed by polishing with a 0.6 μm silica suspension.

Electron backscatter diffraction (EBSD) data of the samples were acquired using an HKL Technology system (Channel 5 software, Oxford Instruments HKL, Hobro, Denmark) coupled with a scanning electron microscope (TESCAN MIRA4 LMH One Max 50) to identify the microstructural changes. The samples for EBSD characterization

Table 2 Creep strain and steady-state creep rate of Zr-4 alloy with and without Cr coating

Creep condition	Primary creep strain/%	Total strain/%	Steady state creep rate/s^{-1}	Creep time/h
350 °C, 117 MPa, coated	0.9	1.03	1.727×10^{-9}	200
350 °C, 117 MPa, uncoated	1.14	1.2	1.522×10^{-9}	200
350 °C, 137 MPa, coated	0.92	1.14	3.820×10^{-9}	200
350 °C, 137 MPa, uncoated	3.04	3.33	4.006×10^{-9}	200
350 °C, 157 MPa, coated	1.52	2.15	8.390×10^{-9}	200
350 °C, 157 MPa, uncoated	5.06	6.9	2.376×10^{-8}	200
350 °C, 177 MPa, coated	3.51	5.18	2.039×10^{-8}	200
350 °C, 177 MPa, uncoated	6.52	11.82	7.154×10^{-8}	200
400 °C, 117 MPa, coated	2.07	2.49	5.127×10^{-9}	200
400 °C, 117 MPa, uncoated	2.81	3.58	9.67×10^{-9}	200
400 °C, 137 MPa, coated	5.92	51.15	1.19×10^{-6}	54.84
400 °C, 137 MPa, uncoated	6.53	62.94	2.42×10^{-6}	29.93
400 °C, 157 MPa, coated	7.62	49.72	3.55×10^{-6}	8.29
400 °C, 157 MPa, uncoated	8.78	66.03	9.67×10^{-6}	7.56

were cut from parallel sections of the dog-bone-shaped samples. These samples were electropolished in a solution of 90 vol.% methanol + 10 vol.% perchloric acid; the polishing voltage and temperature were 20 V and −30 °C (refrigeration with liquid nitrogen), respectively.

Elemental distribution and content characterization were performed using a JXA8230 electron probe microanalyzer (EPMA). The samples for EPMA measurement were mechanically polished using the same method as that used for the SEM samples.

3 Results and discussion

3.1 Microstructure of Cr-coated Zr-4 alloy

The SEM microstructure of the as-received sample is shown in Figs. 2(a−c). The backscattered electron image of the Zr-4 matrix in Fig. 2(a) indicates the absence of precipitates within its matrix. Figures 2(b) and (c) show the microstructure of the Cr coating. A 20 μm-thick Cr coating was deposited onto the surface of the Zr-4 plates. The surface of the coating was dense without any obvious holes and microcracks. However, the cross-sectional images revealed the presence of microcracks and microporosity at the interface of the coating and matrix, which were introduced during the CVD process. Additionally, Fig. 2(d) shows the results of X-ray diffraction patterns. The X-ray peaks of Zr-4 matrix fit the peaks of Zr (hcp), whereas other peaks of precipitates were not detected, in agreement with the results presented in Fig. 2(a). Moreover, the Cr coating did not exhibit any peaks aside from those of Cr (bcc).

The grain size and misorientation angle of the as-received samples are presented in Fig. 3. The microstructure of the Zr-4 matrix, as illustrated in Fig. 3(a), displays equiaxed grains that have a ⟨0001⟩ texture parallel to the normal direction (⟨0001⟩//ND). In Fig. 3(b), the grain boundaries of the Zr-4 matrix are presented, revealing that the majority of these boundaries were characterized as large-angle grain boundaries. The statistical analysis of grain size in Zr-4 matrix is presented in Fig. 3(c), indicating that the majority of grains are smaller than 10 μm. The orientation map of the Cr coating in Fig. 3(d) shows a random orientation without any

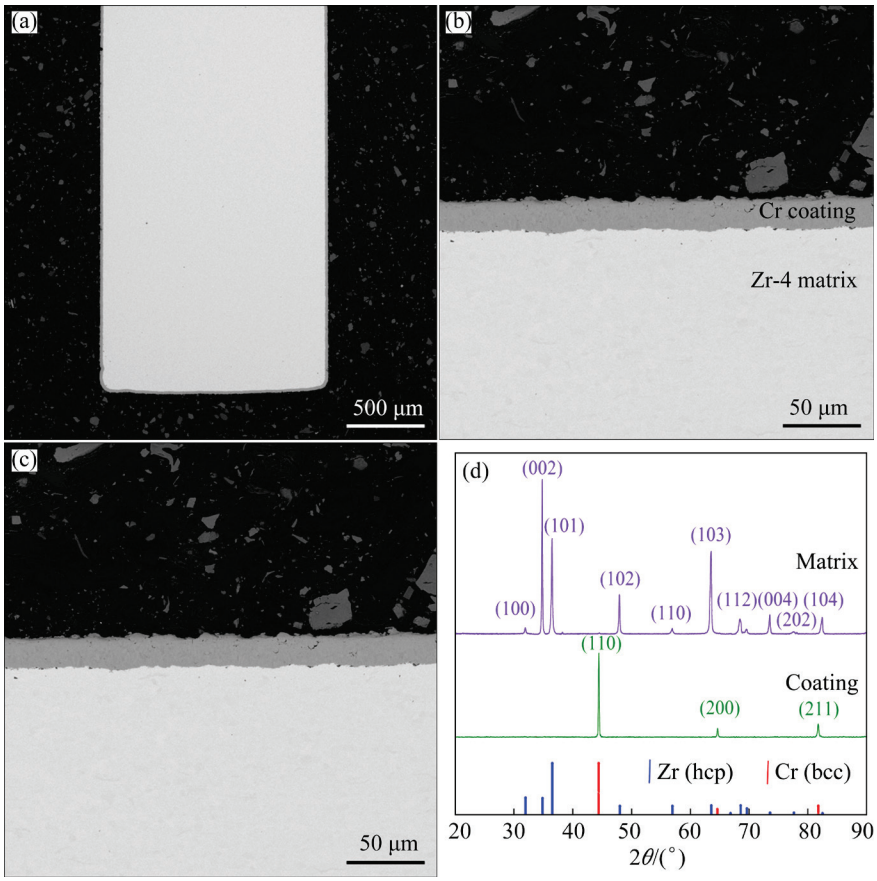

Fig. 2 Microstructures of as-received sample: (a, b) Cross-sectional morphology; (c) Surface morphology; (d) XRD pattern

evident texture. The grains predominantly exhibited a morphology in the form of elongated strips perpendicular to the interface.

3.2 Creep of Cr-coated Zr-4 alloy

The results of the creep tests are shown in Figs. 4 and 5. The three different stages of creep can be observed in Figs. 4(a) and (b). In each creep condition, primary creep was first observed, and all specimens rapidly transitioned to steady-state creep within a few hours of loading. At the onset of the primary creep, under identical experimental conditions, the creep curves of the coated and uncoated samples coincided.

Analysis of the creep behavior of the coated and uncoated samples reveals that during primary creep the total strain of the uncoated sample is higher than that in the coated one. This difference can be observed across a range of different creep conditions but is the most pronounced at the 350 °C and 157 MPa, where the difference in primary strain between the two samples reaches 3.54%. This discrepancy in total creep strain between the coated and uncoated samples suggests that the presence of the coating can mitigate this strain experienced by the material.

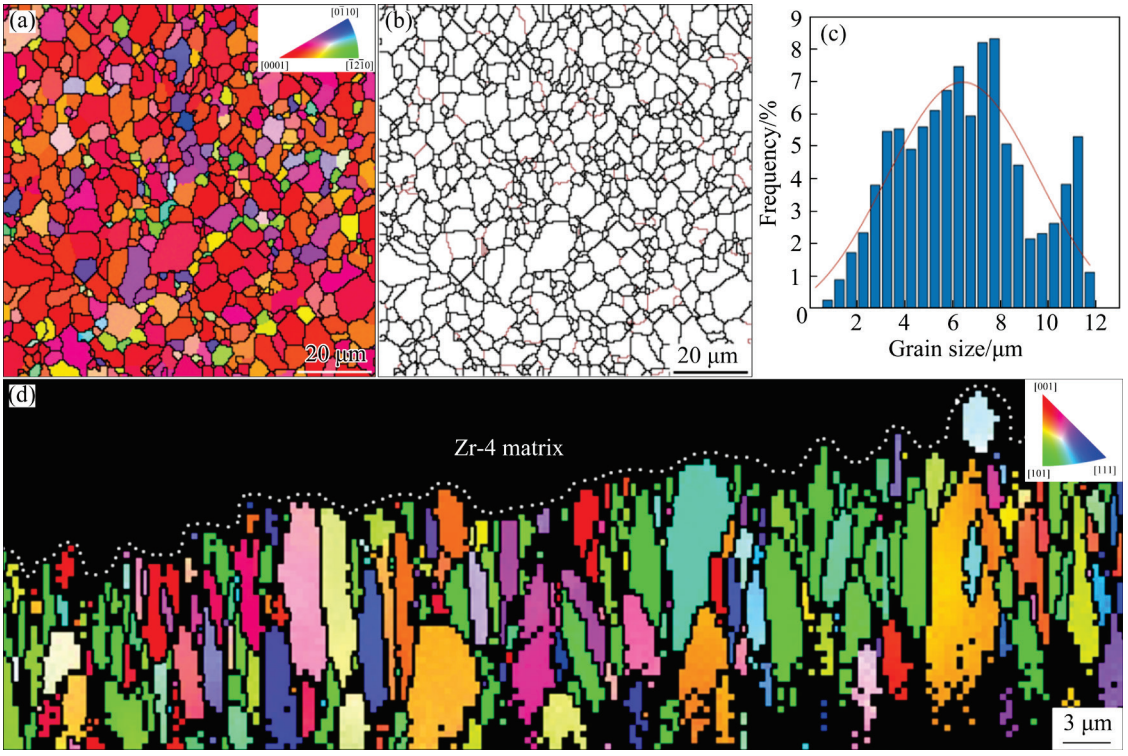

Fig. 3 EBSD images showing microstructure features of as-received sample: (a) Orientation map; (b) Grain boundary map; (c) Grain size distribution of Zr-4 matrix; (d) Orientation map of Cr-coating

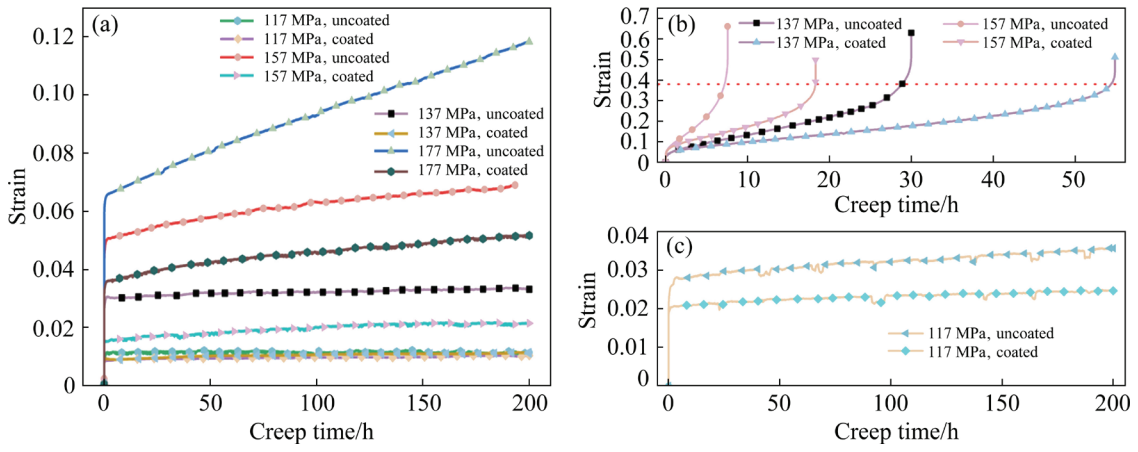

Fig. 4 Creep curves of all tested samples showing strain vs creep time curve at 350 °C (a) and 400 °C (b, c)

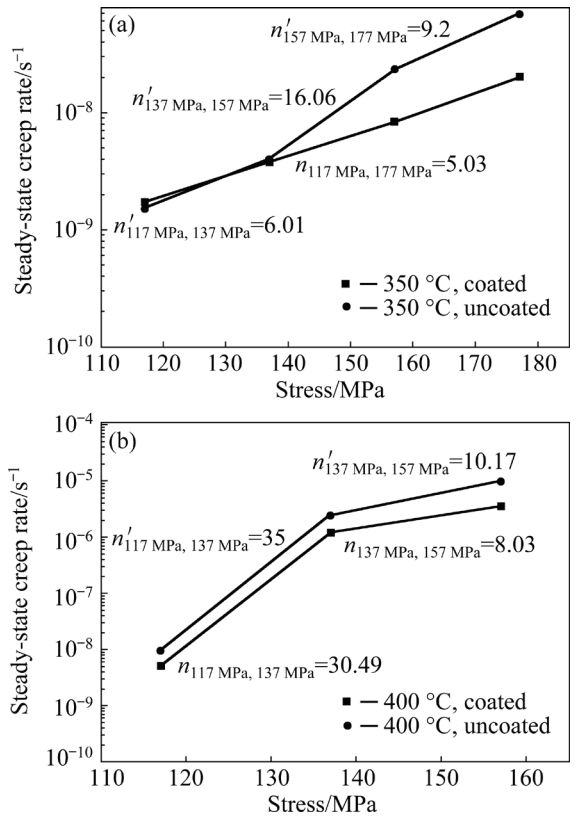

Fig. 5 Relationship between steady-state creep rate and stress at 350 °C (a) and 400 °C (b)

Despite the duration of the experiments, a significant portion of the samples remained in steady-state creep. Thus, we examined their performance in such a stage. The corresponding statistics of the steady-state creep rates for all the samples are presented in Table 2. Furthermore, as illustrated in Figs. 5(a) and (b), the steady-state creep rate increased gradually with the applied stress. Notably, the graphs depict a trend of rapid escalation in the steady-state creep rate upon surpassing a specific stress threshold ($n'_{350\ °C,\ 137\ MPa,\ 157\ MPa}$=16.06, $n'_{400\ °C,\ 117\ MPa,\ 137\ MPa}$=35, $n'_{400\ °C,\ 117\ MPa,\ 137\ MPa}$=30.49). The stress exponent value indicates that the creep follows the dislocation-climb control mechanism ($3<n<8$) and exhibits the power-law breakdown (PLB) with increasing stress.

As the applied stress increases, the effect of the coating on reducing the creep rate during steady-state becomes increasingly notable. At the creep parameters of 350 °C and 117 MPa, the steady-state creep rate exhibits a minor difference (2.05×10^{-10} s^{-1}) between the coated and uncoated samples, which increases to 5.115×10^{-8} s^{-1} when the stress is 177 MPa.

Elevated temperatures also have a pronounced effect on the steady-state creep because the steady-state creep rate at a constant stress level exhibits a positive correlation with temperature. In particular, at 400 °C, the samples underwent power-law breakdown (significant increase in the steady-state creep rate) at 137 MPa.

Drawing upon the analyses of the fracture time in Table 2 as well as Figs. 4 and 5, a comprehensive summary of creep fracture-related information is presented. At lower stress, the sample remains in the steady-state creep for a long time and the occurrence of a fracture is minimal. At 400 °C, the onset of creep fracture was observed during the creep test. The steady-state creep rate rapidly accelerated and transitioned into the tertiary creep stage when the applied stress exceeded 117 MPa. Although both the coated and uncoated samples entered the tertiary creep and experienced creep fracture at higher stress, the coated samples were observed to exhibit superior creep resistance compared with the uncoated ones at equivalent stress levels, exhibiting longer creep fracture time and lower steady-state creep rate. At 400 °C and 137 MPa, the coated sample fractured after 54.84 h, while the uncoated sample fractured only after 29.93 h. Interestingly, all samples essentially fractured at a total strain of 0.3 (red horizontal line); the origin of this effect is explained in the following section.

3.3 Microstructure of Cr-coated Zr-4 alloy after creep

The change of the microstructure before and after creep can explain the difference between the creep properties of the coated and uncoated samples. Figures 6(a) and (b) present the orientation and grain boundary maps, respectively, of the Zr-4 matrix of the coated sample after 200 h creep test conducted at a creep parameter of 400 °C and 117 MPa. The grains of the sample after creep remained equiaxed, and the red-labeled grains that comprise the majority of the total grains clearly indicate the presence of ⟨0001⟩//ND texture. These features are comparable to those observed in the as-received sample, indicating that the grain orientation and grain boundary features after creep remained stable during the creep process. Furthermore, the grain size statistics of the coated

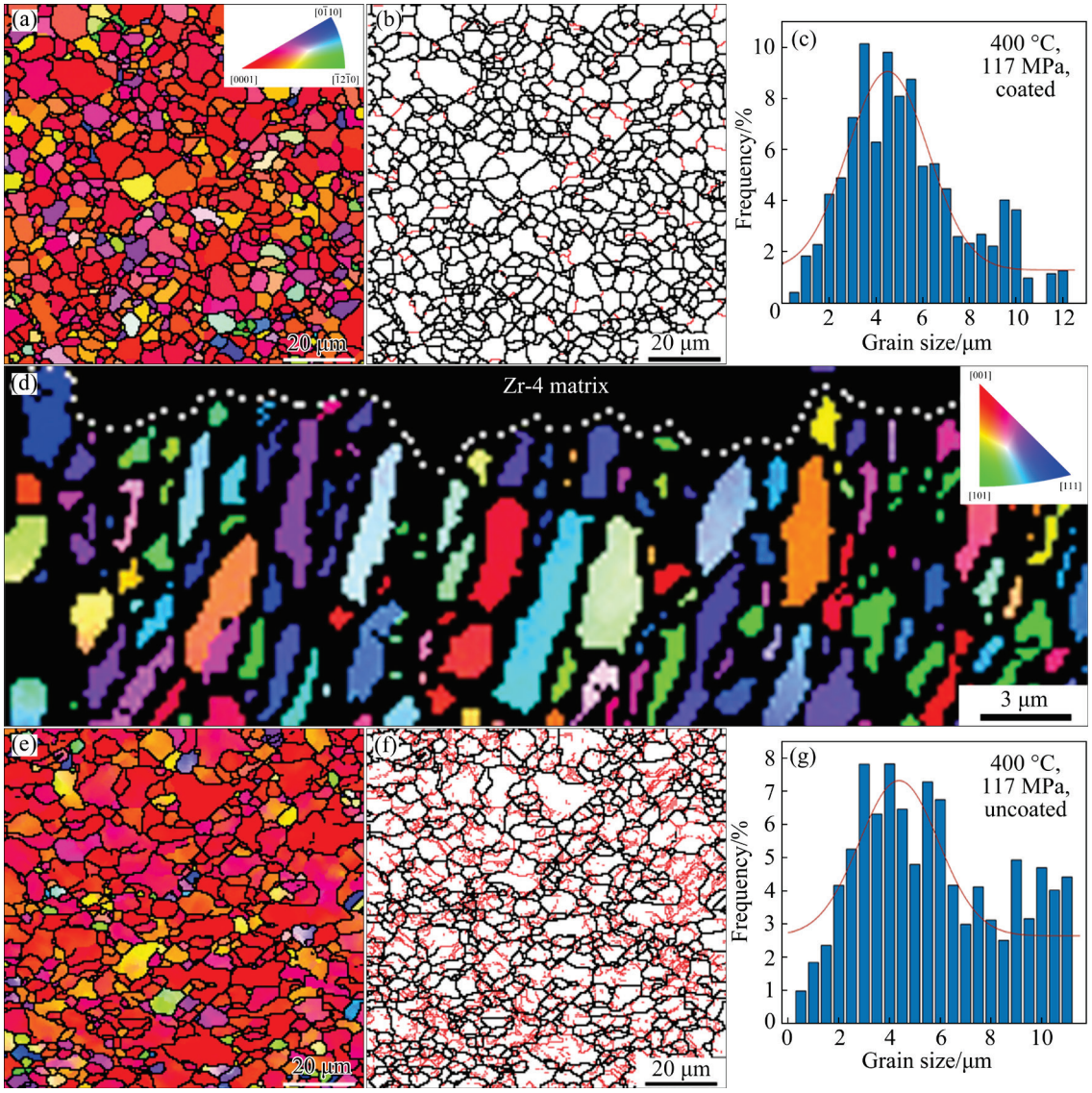

Fig. 6 EBSD orientation maps (a, d, e), grain boundary figures (b, f) and grain size distribution (c, g) of different creep samples at 400 °C and 117 MPa: (a−c) Zr-4 matrix in coated sample; (d) Cr coating; (e−g) Zr-4 matrix in uncoated sample

sample at creep parameters of 400 °C and 117 MPa are summarized in Fig. 6(c). The grain size distribution of the coated and as-received samples are comparable. Additionally, Fig. 6(d) displays the orientation map of the Cr coating, which is similar to that of the as-received sample. These findings collectively suggest that the microstructure of the coated sample remained relatively unchanged during the creep test.

However, notable differences were observed in the matrix of the uncoated sample, as evident in Figs. 6(e−g). Although the orientation (Fig. 6(e)) and grain size distribution (Fig. 6(g)) of the Zr-4 matrix in the uncoated sample at a creep parameter of 400 °C and 117 MPa were similar to those of the coated and as-received samples, a greater density of subgrain boundaries (red regions) appeared within the grains of the Zr matrix in the uncoated sample (Fig. 6(f)).

In fact, the creep process accompanied plastic deformation, further inducing the formation of low misorientation subgrain walls with increase in the total dislocation density. The formation of subgrain boundaries indicates that the creep mechanism under these conditions is associated with a dislocation climb [30,31].

Given that the creep parameters for both the coated and uncoated samples were identical, the

notable difference in microstructure was primarily induced by the presence of the Cr coating.

This result can be further explained by the stress analysis shown in Fig. 7. The stress on the coated sample during creep can be expressed as follows:

$$\sigma_{matrix}S_1+\sigma_{coating}S_2=\sigma_{gross}(S_1+S_2) \quad (3)$$

where σ_{gross} is the loading stress, σ_{matrix} is the stress acting on the matrix, $\sigma_{coating}$ is the stress acting on the coating, S_1 is the cross-sectional area of the matrix, and S_2 is the area of the coating.

In Eq. (3), the term of $\sigma_{matrix}S_1$ denotes the applied creep force on the matrix, and the term of $\sigma_{coating}S_2$ denotes the applied creep force on the coating; thus, $\sigma_{matrix}S_1$ represents the creep force loaded on the matrix, while $\sigma_{coating}S_2$ represents the creep force loaded on the coating. Therefore, the sum of $\sigma_{matrix}S_1$ and $\sigma_{coating}S_2$ is equivalent to the loading force represented by $\sigma_{gross}(S_1+S_2)$.

Assuming strong bonding between the coating and matrix, uniaxial stress would result in equivalent strains in both materials owing to the coordination of deformation between the two. Furthermore, the elastic modulus of the coating is greater than that of the matrix [32], resulting in a higher stress being applied to the coating compared to the matrix under equivalent strain conditions ($\sigma_{coating}>\sigma_{matrix}$).

Given that the stresses are continuously distributed when the coating is well-bonded to the matrix and taking into account the analysis mentioned before, the stress distribution from the coating to the matrix is presented in the stress distribution diagram presented in Fig. 7. The stress distribution diagram illustrates a continuous decrease in stress distribution from the coating to the matrix, transitioning from a high stress to a lower stress at the interface, with the stress magnitude experienced by σ_{matrix} being lower than σ_{gross}. Moreover, the difference in subgrain boundary fraction between the coated and uncoated samples in Fig. 6 corroborates the stress distribution.

3.4 Failure of Cr coating

The surface and cross-sectional morphology of the post-creep samples were characterized, as shown in Fig. 8. Specifically, Figs. 8(a−g) show the SEM images of the coating surface, which reveal the absence of cracks at stress below 157 MPa at 350 °C and below 137 MPa at 400 °C. Moreover, the coating remains well-bonded to the matrix with no evident defects, as deduced from the cross-sectional view. The coating exhibited fractures under certain creep parameters. Specifically, at 300 °C, 157 MPa and 350 °C, 177 MPa, some localized microcracks and microporosities were

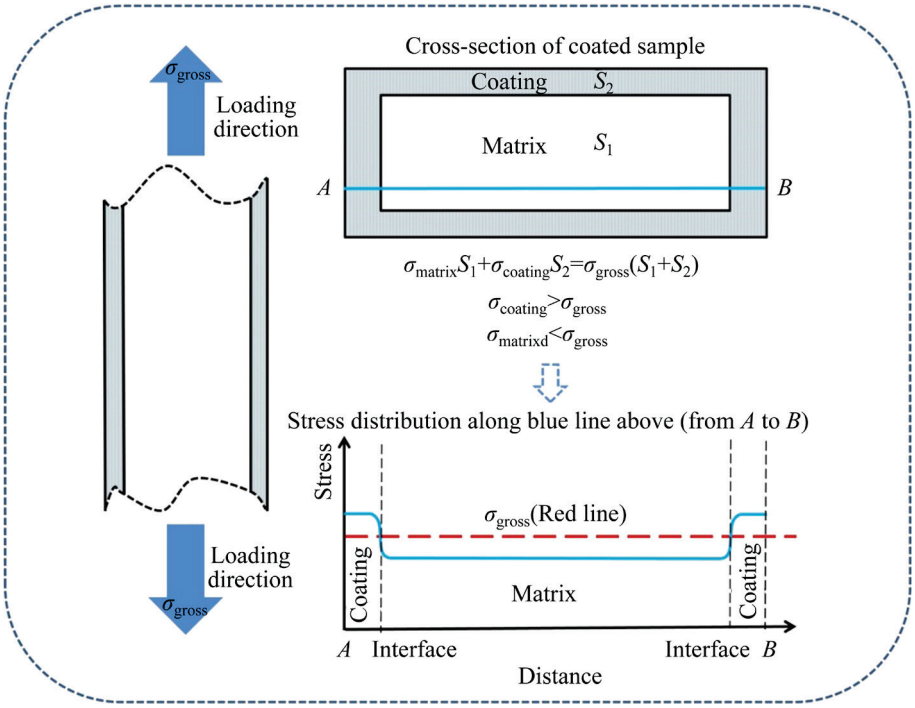

Fig. 7 Stress analysis during creep of coated sample

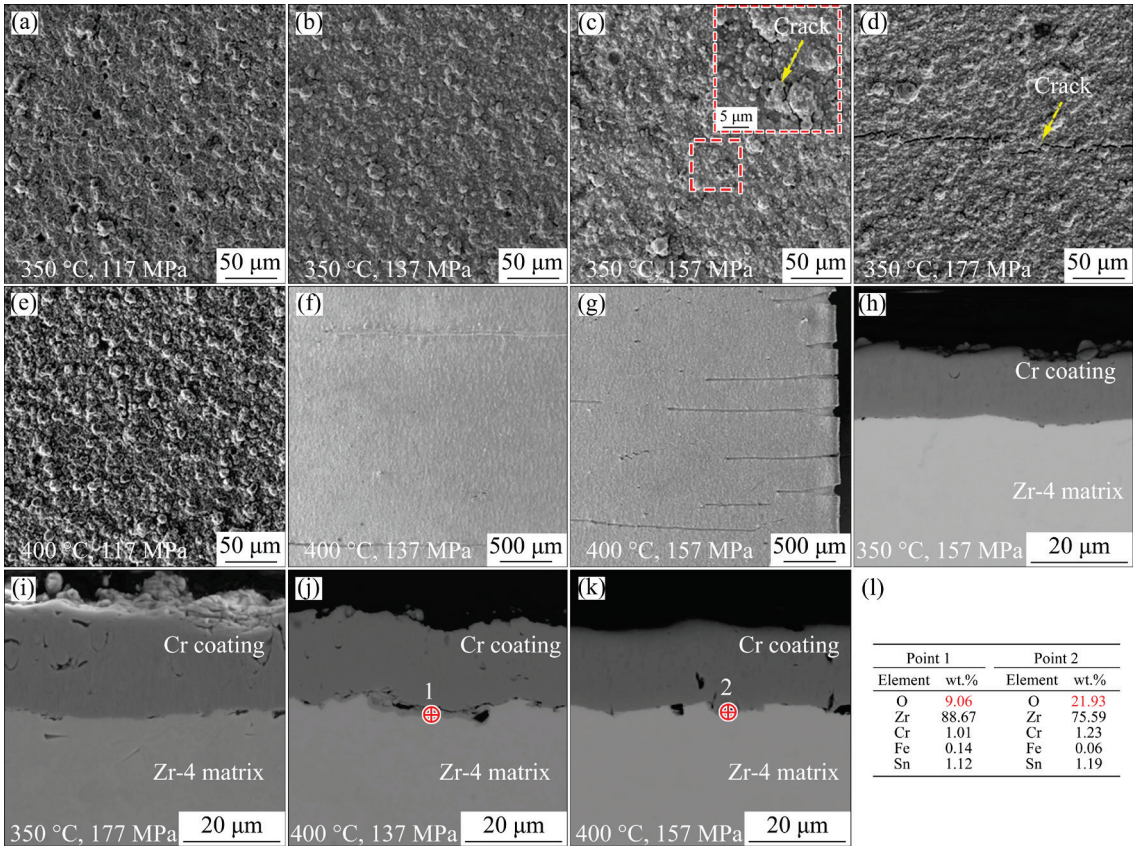

Point 1		Point 2	
Element	wt.%	Element	wt.%
O	9.06	O	21.93
Zr	88.67	Zr	75.59
Cr	1.01	Cr	1.23
Fe	0.14	Fe	0.06
Sn	1.12	Sn	1.19

Fig. 8 Surface morphology of coated samples (a−g), cross-section morphology of coating with cracks under different conditions (h−k), and EDS results (l) in (j) and (k) plots

observed on the coating surface, which had a negligible effect on the steady-state creep rate, as evidenced by a stress exponent of 5.03 in Fig. 5(a). Additionally, the cross-sectional SEM image in Fig. 8 reveals that the unbroken portion of the coating remains well-bonded to the matrix following creep, with a bonding state similar to that of the as-received sample. However, the coating experienced some degree of damage after undergoing creep at 400 °C, 137 MPa and 400 °C, 157 MPa, as evidenced by the emergence of longer cracks on the coating surface (Figs. 8(f, g)) and the presence of breakage or pores in the cross-section (Figs. 8(j, k)). Moreover, based on the results obtained from EPMA scans conducted at Locations 1 and 2 (Figs. 8(j, k)), it is evident that the Zr-4 matrix underwent partial oxidation subsequent to the cracking of the coating. These defects correspond to the abrupt change in the stress exponent presented in Fig. 5(b), wherein the stress exponent of 117−137 MPa at 400 °C (30.49) is abnormally large and significantly exceeds that of power-law creep. Furthermore, the stress exponents obtained from the coated sample creeped under 137−157 MPa at 400 °C (8.03) were found to be considerably lower than those obtained from the sample creeped under 117−137 MPa at 400 °C (30.49), because the sample underwent a transition from a state of high creep resistance (400 °C, 117 MPa) to one of low creep resistance (400 °C, 137 MPa) with an increase of stress from 117 to 137 MPa. This observation provides further evidence for the significant enhancement in the creep resistance of the Zr-4 alloy owing to the presence of the Cr coating.

Despite the observed cracking of coating at 400 °C, the creep resistance of the coated samples remained superior to that of the uncoated samples. The longitudinal section of the fractured coating at 400 °C and 137 MPa is presented in Fig. 9. The angle of fracture with respect to the loading direction is approximately 45°. Several additional cracks were identified near the point of fracture, as shown in Fig. 9(a). Slight oxidation was observed in the vicinity of the crack within the Zr-4 matrix, as illustrated in Figs. 9(a) and (b), whereas the

majority of the matrix exhibited no oxidation, as shown in Figs. 9(a−c). This suggests that despite the damage sustained by the Cr coating during creep, it continued to provide protection to the matrix by not only minimizing the stress but also impeding matrix oxidation.

At elevated temperatures, Cr atoms are prone to diffuse into the Zr-4 matrix during creep, resulting in a gradual reduction of the protective capacity of the Cr coating on the matrix. Moreover, such diffusion can potentially give rise to the formation of intermetallic at the coating−matrix interface, thereby further compromising the protective capacity of the coating. Therefore, to investigate the potential diffusion of Cr into the Zr-4 matrix over extended periods of time, a long-term diffusion test was conducted on the Cr-coated Zr-4 alloy. The EPMA characterization results of the Zr−Cr interface after 1000 h of diffusion at 400 °C are illustrated in Fig. 10, wherein the mass fractions of Zr and Cr are mapped in Figs. 10(a) and (d). Notably, mutual diffusion of Zr and Cr was not observed. Additionally, Figs. 10(b, c) present the mass fraction of Fe and Sn, with a considerable amount of Fe and Sn elements detected in the coating. The Fe content at the interface between the coating and matrix in Fig. 10(b) is nearly identical to that observed in other areas, and intermetallic $Zr(FeCr)_2$ phase was not observed, which were reported in previous studies as a result of high-temperature diffusion [26].

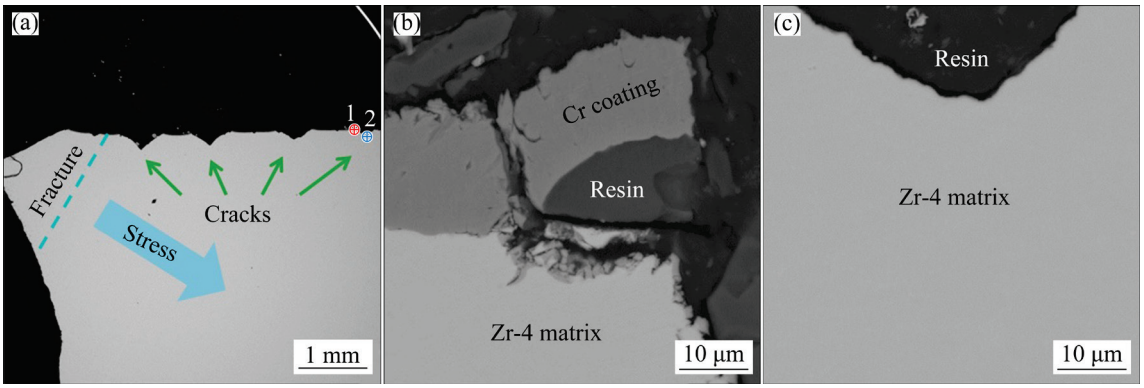

Fig. 9 Longitudinal section morphologies of coated sample creeped at 400 °C and 137 MPa (a), and magnified images of Point 1 (b) and Point 2 (c) in (a)

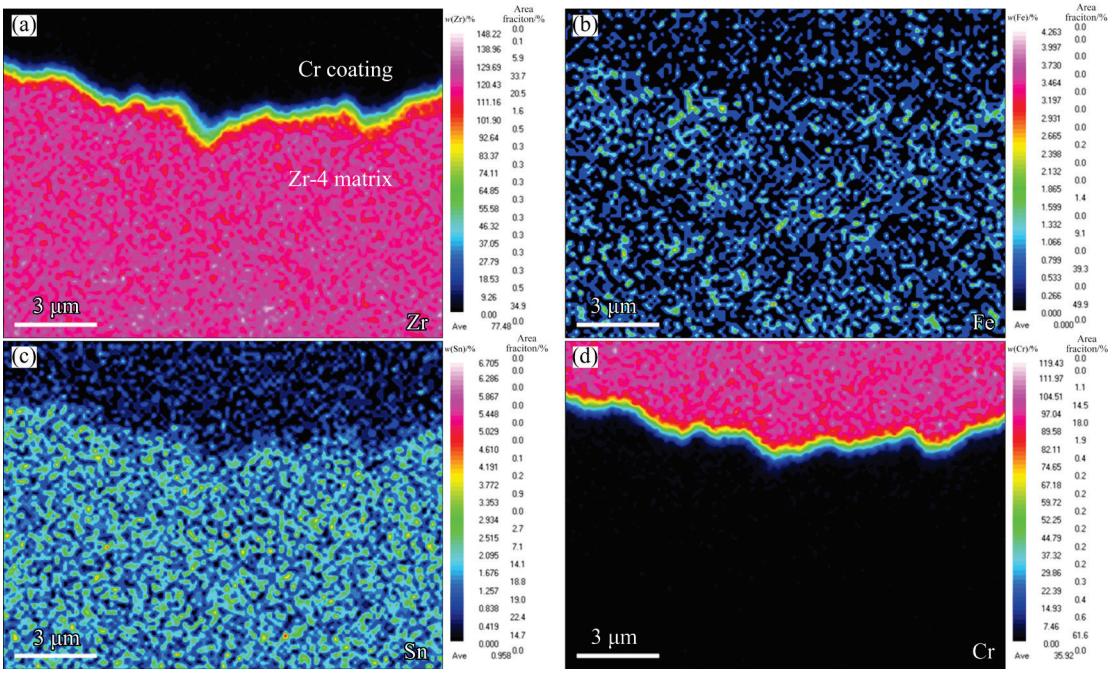

Fig. 10 Element distribution maps of Zr−Cr interface after diffusion at 400 °C for 1000 h

The diffusion coefficient of Cr in the Zr-4 matrix at an elevated temperature of 400 °C is estimated to be 4.461×10^{-18} m^2/s [33], which suggests that the mutual diffusion of Cr and Zr is hindered at this temperature. Moreover, if Sn and Fe migrate from the Zr matrix to the Cr coating, the bonding between the coating and the matrix would be strengthened, leading to solid-solution strengthening of the coating. Consequently, long-term diffusion at 400 °C could potentially suppress the cracking of the coating under high stress and enhance the creep resistance of the Zr-4 alloy.

3.5 Creep fracture feature

The fracture surface morphology of the Cr-coated Zr-4 alloy at 400 °C and 137 MPa was characterized. The overview fracture surface is shown in Fig. 11(a), which reveals that the central part of the fracture is rugged and decorated with pores, while the edges are smooth. Further, magnified SEM images of the region marked by red boxes 1, 2, and 3 in Fig. 11(a) are presented in Figs. 11(b−d), respectively. In Fig. 11(b), ductile dimples are observed dominating the central region, indicating good ductility of the matrix. The ductile dimples and pores observed in the central region indicate that the fracture resulted from the nucleation of cavities followed by growth. At the edge region in Fig. 11(c), a mixed fracture style is observed, including dimples and cleavage fracture. Finally, the magnified SEM image of the region marked by red box 3 in Fig. 11(a) shows that cleavage dominates this area.

Based on the aforementioned observations, the mechanism of creep fracture can be inferred. Specifically, under high stress conditions, the coating experiences a rupture failure, which causes an increase in the stress on the Zr-4 matrix. Subsequently, nucleation of cavities takes place within the matrix, which gradually grow until the sample undergoes fracture.

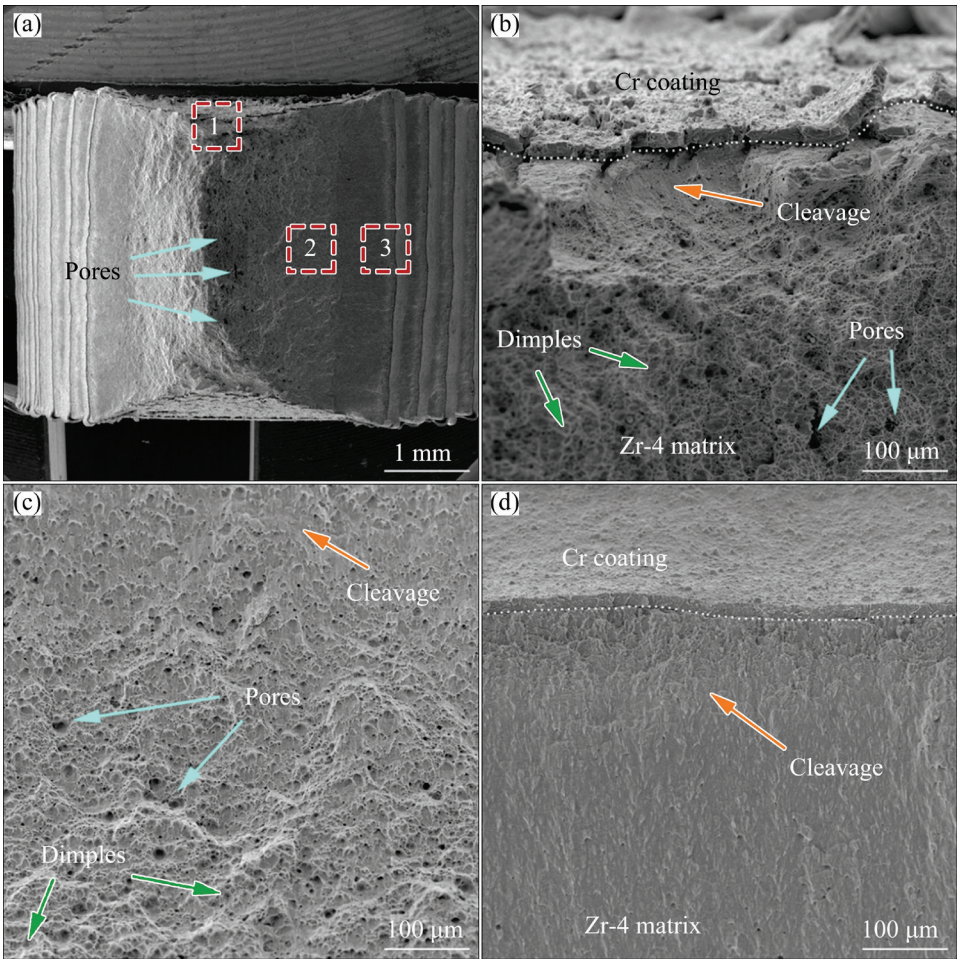

Fig. 11 Creep fracture morphology of Cr-coated Zr-4 alloy at 400 °C and 137 MPa (a), and magnified images of Area 1 (b), Area 2 (c) and Area 3 (d) in (a)

3.6 Comparison of creep fracture life of typical nuclear cladding materials

The fracture analysis and creep curves presented in Fig. 4 show that the fracture feature of the sample after the coating breakage is similar to that of the uncoated sample. All fractured samples entered tertiary creep stage at an approximately identical strain (red-horizontal-dashed line in Fig. 4(b)) that fits well with the Monkman–Grant relationship [27] for creep fracture given by Eq. (2). The creep fracture time in Eq. (3) is a dependent variable of the steady-state creep rate. Since N is a constant, Eq. (3) can be expressed as

$$N\lg \dot{\varepsilon}_{ss} + \lg t_f = \lg k_{MG} \quad (4)$$

Therefore, t_f varies linearly with $\dot{\varepsilon}_{ss}$ in the double logarithmic coordinate system. Since the creep fracture of the coated Zr-4 alloy follows the Monkman–Grant relationship, we can deduce the fitting curve (black line in Fig. 12) with a coefficient of determination (R^2) of 0.996 for the creep rate versus fracture time based on the measured steady-state creep rate as well as the fracture time in this study. We derive the following relationship:

$$\dot{\varepsilon}_{ss}^{0.957} t_f = 0.429 \quad (5)$$

The experimental data and fitted curve in this study and the data for other typical nuclear cladding materials such as SiC_f/SiC, FeCrAl(ODS), and nickel alloys are shown in Fig. 12.

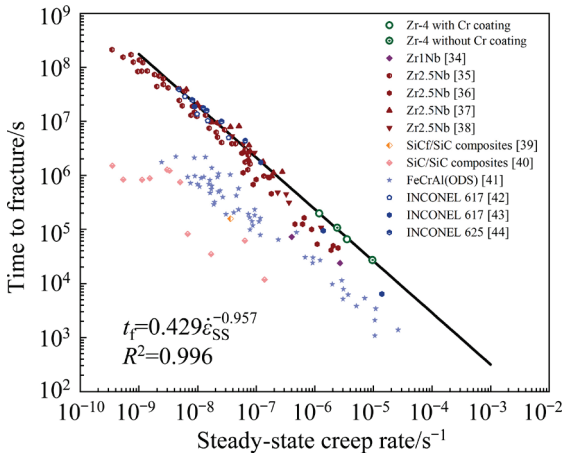

Fig. 12 Creep fracture time vs steady-state creep rate of Cr-coated Zr-4 alloy and other typical cladding materials

The collected Zr data from the previous studies [34−38] are mostly distributed in close proximity to the fitted curve, indicating that the fracture time of the coated sample is comparable to that of other Zr alloys, commonly used as cladding materials. However, data points situated below the fitted black line suggest that those materials exhibit a shorter fracture time than the coated Zr-4 alloy under the same steady-state creep rate. This observation highlights the excellent high-temperature creep fracture resistance of the Cr-coated Zr-4 alloy in comparison with the majority of nuclear cladding materials employed in nuclear reactors, as well as the Inconel alloy utilized in high-temperature structures [34−44].

4 Conclusions

(1) Compared with the uncoated Zr-4 alloy, the Zr-4 alloy with a Cr coating exhibited a significant enhancement in its creep resistance. The subgrain boundary fraction observed in the coated samples was lower than that in the uncoated samples after the creep test, signifying that the Cr coating minimized the stress on the Zr-4 matrix.

(2) The Cr coating exhibits high stability during long-term diffusion test. Cracking of the Cr coating occurred under a minimum stress of 157 MPa at 350 °C and 137 MPa at 400 °C.

(3) The fracture time of the Cr-coated sample was fitted with the Monkman−Grant relationship, obtaining $\dot{\varepsilon}_{ss}^{0.957} t_f = 0.429$. The results could be useful in predicting the creep fracture time of Cr-coated Zr-4 cladding materials.

CRediT authorship contribution statement

Ding ZUO: Investigation, Methodology, Writing − Origin-draft, Writing − Review & editing; **Pei-nan DU:** Formal analysis, Writing − Review & editing; **Wei LUO:** Investigation, Formal analysis, Writing review; **Huan CHEN:** Data curation, Formal analysis; **Yu WANG:** Investigation, Formal analysis; **Tian-guo WEI:** Investigation, Data curation; **Rui-qian ZHANG:** Resource, Project administration; **Hui-qun LIU:** Supervision, Funding acquisition, Writing − Review & editing.

Declaration of competing interest

The authors declare that they have no known competing financial interests or personal relationships that could have appeared to influence the work reported in this paper.

Acknowledgments

This research was funded by the Key Project of

Nuclear Safety and Advanced Nuclear Technology, China (No. 2019YFB1901002), and the Project supported by the State Key Laboratory of Powder Metallurgy, Central South University, China.

References

[1] NORTHWOOD D O. The development and applications of zirconium alloys [J]. Materials & Design, 1985, 6(2): 58−70.

[2] JIANG Hai-xia, DUAN Ze-wen, ZHANG Bei-bei, ZHAO Xiao-yu, WANG Peng. Wear behavior of zirconium-4 alloy after different irradiation damage level [J]. Applied Surface Science, 2020, 509: 145373.

[3] HAYES T A, KASSNER M E. Creep of zirconium and zirconium alloys [J]. Metallurgical and Materials Transactions A, 2006, 37: 2389−2396.

[4] LE S M, BRACHET J C, VANDENBERGHE V, AMBARD A, CHOSSON R. Breakaway oxidation of zirconium alloys exposed to steam around 1000 °C [J]. Corrosion Science, 2020, 176: 108936.

[5] ZINKLE S J, TERRANI K A, GEHIN J C, OTT L J, SNEAD L L. Accident tolerant fuels for LWRs: A perspective [J]. Journal of Nuclear Materials, 2014, 448(1/2/3): 374−379.

[6] BRAGG-SITTON S M, TODOSOW M, MONTGOMERY R, STANEK C R, MONTGOMERY R, CARMACK W J. Metrics for the technical performance evaluation of light water reactor accident-tolerant fuel [J]. Nuclear Technology, 2016, 195(2): 111−123.

[7] KONG De-cheng, DONG Chao-fang, XIAO Kui, LI Xiao-gang. Effect of temperature on copper corrosion in high-level nuclear waste environment [J]. Transactions of Nonferrous Metals Society of China, 2017, 27(6): 1431−1438.

[8] KIM H G, YANG J H, KIM W J, KOO Y H. Development status of accident-tolerant fuel for light water reactors in Korea [J]. Nuclear Engineering and Technology, 2016, 48(1): 1−15.

[9] LI Chang, WANG Hong-lei, YANG Ya-ping, GU Quan-chao, YAN Xing-heng, ZHOU Xin-gui. Blast and tensile properties of tantalum/niobium lined SiC/SiC composite tubes for nuclear cladding [J]. Transactions of Nonferrous Metals Society of China, 2022, 32(6): 1961−1968.

[10] DRYEPONDT S, UNOCIC K A, HOELZER D T, MASSEY C P, PINT B A. Development of low-Cr ODS FeCrAl alloys for accident-tolerant fuel cladding [J]. Journal of Nuclear Materials, 2018, 501: 59−71.

[11] GAMBLE K A, BARANI T, PIZZOCRI D, HALES J D, TERRANI K A, PASTORE G. An investigation of FeCrAl cladding behavior under normal operating and loss of coolant conditions [J]. Journal of Nuclear Materials, 2017, 491: 55−66.

[12] CHEN Huan, WANG Xiao-ming, ZHANG Rui-qian. Application and development progress of Cr-based surface coatings in nuclear fuel element: I. Selection, preparation, and characteristics of coating materials [J]. Coatings, 2020, 10(9): 808.

[13] YOUNG D J. High temperature oxidation and corrosion of metals [M]//Corrosion Series, Amsterdam: Elsevier, 2008.

[14] BIRKS N, MEIER G H, PETTIT F S. Introduction to the high temperature oxidation of metals [M]. Cambridge, UK: Cambridge University Press, 2006.

[15] TERRANI K A. Accident tolerant fuel cladding development: Promise, status, and challenges [J]. Journal of Nuclear Materials, 2018, 501: 13−30.

[16] PARISH C M, UNOCIC K A, TAN L, ZINKLE S J, KONDO S, SNEAD L L, HOELZER D T, KATOH Y. Helium sequestration at nanoparticle-matrix interfaces in helium + heavy ion irradiated nanostructured ferritic alloys [J]. Journal of Nuclear Materials, 2017, 483: 21−34.

[17] DAUB K, VAN NIEUWENHOVE R, NORDIN H. Investigation of the impact of coatings on corrosion and hydrogen uptake of Zircaloy-4 [J]. Journal of Nuclear Materials, 2015, 467: 260−270.

[18] TANG C C, STUEBER M, SEIFERT H J, STEINBRUECK M. Protective coatings on zirconium-based alloys as accident-tolerant fuel (ATF) claddings [J]. Corrosion Reviews, 2017, 35(3): 141−165.

[19] ŠEVEČEK M, GURGEN A, SESHADRI A, CHE Y F, WAGIH M, PHILLIPS B, CHAMPAGNE V, SHIRVAN K. Development of Cr cold spray–coated fuel cladding with enhanced accident tolerance [J]. Nuclear Engineering and Technology, 2018, 50(2): 229−236.

[20] BRACHET J C, IDARRAGA-TRUJILLO I, LE FLEM M, et al. Early studies on Cr-Coated Zircaloy-4 as enhanced accident tolerant nuclear fuel claddings for light water reactors [J]. Journal of Nuclear Materials, 2019, 517: 268−285.

[21] WEI Tian-guo, ZHANG Rui-qian, YANG Hong-yan, LIU Hong, QIU Shao-yu, WANG Yu, DU Pei-nan, HE Kun, HU Xiao-gang, DONG Chuang. Microstructure, corrosion resistance and oxidation behavior of Cr-coatings on Zircaloy-4 prepared by vacuum arc plasma deposition [J]. Corrosion Science, 2019, 158: 108077.

[22] KUPRIN A S, BELOUS V A, VOYEVODIN V N, VASILENKO R L, OVCHARENKO V D, TOLSTOLUTSKAYA G D, KOPANETS I E, KOLODIY I V. Irradiation resistance of vacuum arc chromium coatings for zirconium alloy fuel claddings [J]. Journal of Nuclear Materials, 2018, 510: 163−167.

[23] BRACHET J C, ROUESNE E, RIBIS J, et al. High temperature steam oxidation of chromium-coated zirconium-based alloys: Kinetics and process [J]. Corrosion Science, 2020, 167: 108537.

[24] MA Hai-bin, YAN Jun, ZHAO Ya-huan, LIU Tong, REN Qi-sen, LIAO Ye-hong, ZUO Jia-dong, LIU Gang, YAO Mei-yi. Oxidation behavior of Cr-coated zirconium alloy cladding in high-temperature steam above 1200 °C [J]. NPJ Materials Degradation, 2021, 5(1): 7.

[25] LI Qing, SONG Peng, ZHANG Rui-qian, LI Zhen-hua, WANG Yu, DU Pei-nan, LU Jian-sheng. Oxidation behavior and Cr-Zr diffusion of Cr coatings prepared by atmospheric plasma spraying on zircaloy-4 cladding in steam at 1300 °C [J]. Corrosion Science, 2022, 203: 110378.

[26] YANG Jian-qiao, STEGMAIER U, TANG Chong-chong, STEINBRÜCK M, GROßE M, WANG Shu-zhong, SEIFERT H J. High temperature Cr−Zr interaction of two types of Cr-coated Zr alloys in inert gas environment [J]. Journal of Nuclear Materials, 2021, 547: 152806.

[27] KASSNER M E. Fundamentals of creep in metals and alloys [M]. Butterworth-Heinemann, 2015.
[28] EVANS H E. Mechanisms of creep fracture [M]. London: Elsevier Applied Science Publishers, 1984.
[29] ADAMSON R B, COLEMAN C E, GRIFFITHS M. Irradiation creep and growth of zirconium alloys: A critical review [J]. Journal of Nuclear Materials, 2019, 521: 167−244.
[30] SHERBY O D, TALEFF E M. Influence of grain size, solute atoms and second-phase particles on creep behavior of polycrystalline solids [J]. Materials Science and Engineering: A, 2002, 322(1/2): 89−99.
[31] SHERBY O D, BURKE P M. Mechanical behavior of crystalline solids at elevated temperature [J]. Progress in Materials Science, 1968, 13: 323−390.
[32] QI Fei-peng, LIU Zhen-hai, LI Quan, YU Hong-xing, CHEN Ping, LI Yuan-ming, ZHOU Yi, MA Chao, TANG Chang-bing, HUANG Yong-zhong, ZHAO Bo, LU Huai-yu. Pellet-cladding mechanical interaction analysis of Cr-coated Zircaloy cladding [J]. Nuclear Engineering and Design, 2020, 367: 110792.
[33] BALART S N, VARELA N, de TENDLER R H. 51Cr diffusion in α-Zr single crystals [J]. Journal of Nuclear Materials, 1983, 119(1): 59−66.
[34] SKLENICKA V, KRAL P, KUCHAROVA K, KVAPILOVA M, DVORAK J, KLOC L. Thermal creep fracture of a Zr1% Nb cladding alloy in the α and (α+β) phase regions [J]. Journal of Nuclear Materials, 2021, 553: 152950.
[35] GOPALAN A, PATEL V, KHANDELWAL H K, DEVI Y P, SINGH R N. Effect of manufacturing route on thermal creep behaviour of Zr−2.5Nb pressure tube alloy used in Indian PHWR [J]. Journal of Nuclear Materials, 2022, 569: 153903.
[36] SKLENICKA V, DVORAK J, KRAL P, BETEKHTIN V I, KADOMTSEV A G, NARYKOVA M V, DOBATKIN S V, KUCHAROVA K, KVAPILOVA M. Influence of a prior pressurization treatment on creep behaviour of an ultrafine-grained Zr−2.5%Nb alloy [J]. Materials Science and Engineering: A, 2021, 820: 141570.
[37] GUGULOTH K, GHOSH M, SWAMINATHAN J, MITRA R. Tensile creep and rupture behavior along with evolution of microstructure in a Zr−2.5Nb alloy [J]. Materials Science and Engineering A, 2020, 791: 139681.
[38] GUGULOTH K, MITRA R, CHOWDHURY S G, SWAMINATHAN J. Mechanism of creep deformation with evolution of microstructure and texture of Zr−2.5Nb alloy [J]. Materials Science and Engineering: A, 2018, 721: 286−302.
[39] ALMANSOUR A S, MORSCHER G N. Tensile creep behavior of SiC_f/SiC ceramic matrix minicomposites [J]. Journal of the European Ceramic Society, 2020, 40(15): 5132−5146.
[40] BHATT R T, KISER J D. Creep behavior and failure mechanisms of CVI and PIP SiC/SiC composites at temperatures to 1650 °C in air [J]. Journal of the European Ceramic Society, 2021, 41(13): 6196−6206.
[41] UKAI S, KATO S, FURUKAWA T, OHTSUKA S. High-temperature creep deformation in FeCrAl-oxide dispersion strengthened alloy cladding [J]. Materials Science and Engineering A, 2020, 794: 139863.
[42] CHOI J, NETO L B, WRIGHT R N, KRUZIC J J, MURÁNSKY O. On the prediction of creep behaviour of alloy 617 using Kachanov-Rabotnov model coupled with multi-objective genetic algorithm optimisation [J]. International Journal of Pressure Vessels and Piping, 2022, 199: 104721.
[43] WRIGHT J K, LILLO T M, WRIGHT R N, KIM W G, SAH I J, KIM E S, PARK J Y, KIM M H. Creep and creep-rupture of Alloy 617 [J]. Nuclear Engineering and Design, 2018, 329: 142−146.
[44] SON K T, PHAN T Q, LEVINE L E, KIM K S, LEE K A, AHLFORS M, KASSNER M E. The creep and fracture properties of additively manufactured inconel 625 [J]. Materialia, 2021, 15: 101021.

Cr 涂层对 Zr-4 合金蠕变行为的影响

左 鼎[1]，杜沛南[2]，罗 威[1]，陈 寰[2]，王 昱[2]，韦天国[2]，张瑞谦[2]，刘会群[1,3]

1. 中南大学 材料科学与工程学院，长沙 410083；
2. 中国核动力研究设计院 反应堆燃料及材料重点实验室，成都 610213；
3. 中南大学 粉末冶金国家重点实验室，长沙 410083

摘 要：报道化学气相沉积 Cr 涂层对 Zr-4 合金蠕变性能的影响以及 Cr 涂层在服役温度下的热稳定性。利用扫描电镜、电子探针显微分析和电子背散射衍射研究样品的显微组织。结果表明：样品 Zr-4 基体中晶粒呈等轴状，存在明显的⟨0001⟩//ND 织构。蠕变后涂层样品的 Zr-4 合金基体中亚晶界数量明显低于无涂层样品 Zr-4 合金基体中亚晶界数量，表明 Cr 涂层显著降低了 Zr-4 合金基体在蠕变过程中承载的应力，提高了合金的抗蠕变性能。Cr 涂层在长时间扩散实验中保持高稳定性。涂层在高蠕变应力下(350 ℃时不小于 157 MPa，400 ℃时不小于 137 MPa)出现裂纹。系统总结蠕变断裂的数据，得到了关于稳态蠕变速率与蠕变断裂时间的 Monkman−Grant 关系式。

关键词：Zr-4 合金；Cr 涂层；蠕变行为；显微组织；热稳定性

(Edited by Xiang-qun LI)